Front. Chem. Sci. Eng. 2022, 16(12): 1772−1781
https://doi.org/10.1007/s11705-022-2197-4

RESEARCH ARTICLE

Spin polarization strategy to deploy proton resource over atomic-level metal sites for highly selective CO_2 electrolysis

Yingjie Zhao[1], Xinyue Wang[1], Xiahan Sang[3], Sixing Zheng[1], Bin Yang[1,2], Lecheng Lei[1,2], Yang Hou[1,2], Zhongjian Li (✉)[1,2]

1 Key Laboratory of Biomass Chemical Engineering of Ministry of Education, College of Chemical and Biological Engineering, Zhejiang University, Hangzhou 310027, China
2 Institute of Zhejiang University-Quzhou, Quzhou 324000, China
3 Nanostructure Research Centre, Wuhan University of Technology, Wuhan 430070, China

© Higher Education Press 2022

Abstract Unlocking of the extremely inert C=O bond during electrochemical CO_2 reduction demands subtle regulation on a key "resource", protons, necessary for intermediate conversion but also readily trapped in water splitting, which is still challenging for developing efficient single-atom catalysts limited by their structural simplicity usually incompetent to handle this task. Incorporation of extra functional units should be viable. Herein, a proton deployment strategy is demonstrated via "atomic and nanostructured iron (A/N-Fe) pairs", comprising atomically dispersed iron active centers spin-polarized by nanostructured iron carbide ferromagnets, to boost the critical protonation steps. The as-designed catalyst displays a broad window (300 mV) for CO selectivity > 90% (98% maximum), even outperforming numerous cutting-edge M–N–C systems. The well-placed control of proton dynamics by A/N-Fe can promote *COOH/*CO formation and simultaneously suppress H_2 evolution, benefiting from the magnetic-proximity-induced exchange splitting (spin polarization) that properly adjusts energy levels of the Fe sites' *d*-shells, and further those of the adsorbed intermediates' antibonding molecular orbitals.

Keywords CO_2 electrolysis, single-atom catalysts, spin polarization, proton dynamics, *in situ* IR spectroscopy, kinetic isotope effect

1 Introduction

Direct usage of intermittent renewable energy in electrochemical CO_2 reduction reaction (CO_2RR) is one of the greenest routes to large-scale production of value-added chemicals for sustainable carbon cycle [1]. Despite attractive prospects, it faces fiendish puzzles thrown by the extremely inert C=O bond (806 $kJ \cdot mol^{-1}$), doomed to undergo complex elementary steps one by one ($CO_2 \rightarrow CO$, for instance; the asterisk denotes the active site) [2,3]:

$$* + CO_2 + e^- \rightarrow *CO_2^{\bullet -} \quad (1)$$

$$*CO_2^{\bullet -} + H^+ \rightarrow *COOH \quad (2)$$

$$*COOH + H^+ + e^- \rightarrow *CO + H_2O \quad (3)$$

$$*CO \rightarrow * + CO \quad (4)$$

To whizz down the above stages, the whereabouts of a key species, protons, deserve special attention: one destination is to serve as propellant to attack oxygen atom off the intermediates and launch CO_2-to-CO conversion, while the other is reactant of the parasitic hydrogen evolution reaction (HER) [4]. How to reinforce the former and stifle the latter is the crux of selectivity conundrum. Novel, high-performance CO_2RR electrocatalysts, therefore, ought to undertake double mission of reducing activation barrier, and addressing this proton-dominated kinetic conflict [5,6].

Carbon-based single-atom catalysts (SACs), composed of homogeneous, well-defined transition metal-nitrogen (TM-N) moieties, have demonstrated striking activity for CO_2RR to yield CO [7,8]. Nevertheless, their biggest drawback exactly lies in the structural simplicity usually only amenable to single molecule [9,10], leaving little leeway to deploy "proton resource". This seriously harms the bimolecular proton-coupled electron transfer (PCET), and thus the chances of *COOH/*CO formation [11,12]. Besides, consider one possible scenario wherein poor proton utilization caused by slow CO_2 reduction rate engenders an excessive accumulation of protons [13], or

Received April 14, 2022; accepted May 21, 2022

E-mail: zdlizj@zju.edu.cn

figuratively, proton flooding. Absent a forceful restriction—what the single-site nature sacrifices, these surplus protons not participated in intermediate protonation will be compelled to turn to the unpleasing HER readily under overpotential driving force, degrading CO_2RR. Hence, appropriate function should be loaded into SACs to constrain the double-edged-sword protons, as a "dispatcher" to delicately plan their dynamics of moving toward not H_2 but solely CO_2 [14,15]. For a representative category, Fe–N–C, the strong bonding of *CO to Fe center often prevents its escape and thus the next opening of CO_2-to-CO [16], responsible for a deficiency of newly formed CO_2RR intermediates to consume protons. This imperfection, plus the sluggish PCETs, will further exacerbate and magnify proton flooding indeed, but which, from another aspect, makes Fe–N–C a suitable platform to investigate an elegant proton deployment strategy applicable for SAC systems.

Herein, to implement this concept, we engineer atomic and nanostructured iron (A/N-Fe) pairs anchored on N-doped carbon nanosheet, consisting of isolated active iron atoms coupled with nanostructured iron carbide. The best-performing catalyst achieves a low initial potential at –0.20 V and a maximal CO Faradaic efficiency (FE_{CO}) of 98% (FE_{CO} > 90% spanning 300 mV). Density functional theory (DFT) calculations manifest a built-in spin polarization throughout the A/N-Fe, which draws an ideal electronics blueprint for precisely CO_2RR-targeted proton deployment. Kinetic analyses verify that the unique constraint effect by A/N-Fe can navigate protons to *CO_2/*COOH conversion while obstruct the branch to H_2 evolution, whereas single-atom Fe (SA-Fe) alone falls short of such goals.

2 Experimental

2.1 Computational methodologies

Theoretical prediction was performed by first-principle calculations within DFT framework, as implemented in the plane-wave basis set Vienna ab initio Simulation Package code. Models and methods are given in Fig. S1 (cf. Electronic Supplementary Material, ESM) and Text S1 (cf. ESM).

2.2 Catalyst synthesis

Fe_3C-X@Fe-NC series. The procedure includes prearranged hemin–melamine crosslinking network as precursor and subsequent slow-rate thermal pyrolysis under N_2 atmosphere [17]. Fe_3C-X@Fe-NCs (X = S, M and L, abbreviation of small, middle and large, respectively, represents the proportion of condensed- vs. isolated-iron, denoted N_{Fe}/A_{Fe}), which host a union of Fe_3C nanoparticles and Fe-N_x moieties, were prepared at specific anneal temperatures (Fig. 1). The detailed process is given in Text S3 (cf. ESM).

Fe-NC. To prepare Fe-NC with only atomic-level Fe species, the temperature just mentioned was set below the threshold of Fe_3C formation. The detailed process is given in Text S4 (cf. ESM).

FeC@C. To prepare FeC@C with only nanostructured Fe species, pure instead of N-doped carbon matrix was used as the support to grow Fe_3C under CO atmosphere [18], which ensures that isolated Fe atoms would not be formed since there is no N atom to serve as the anchor to fix them. The detailed process is given in Text S5 (cf. ESM).

NC. To prepare NC without Fe species, the hemin used for Fe_3C-X@Fe-NC and Fe-NC was replaced by metal-free pyromellitic acid. This makes it practicable to avoid introducing iron source and to maintain crosslinking network of the precursor [19]. The detailed process is given in Text S6 (cf. ESM).

2.3 Material characterization

Details of the physical and electrochemical characterizations are given in Texts S7–S9 (cf. ESM). All the electrochemical CO_2RR performances were measured in a three-electrode H-cell containing CO_2-saturated 0.5 $mol \cdot L^{-1}$ $KHCO_3$ aqueous electrolyte.

2.4 Kinetics analyses

Kinetics analyses include *in situ* attenuated total reflectance surface enhanced infrared absorption spectroscopy (ATR-SEIRAS) and kinetic isotope effect (KIE) study. Test parameters of the ATR-SEIRAS are given in Text S10 (cf. ESM). For KIE study, the CO_2RR in deuterated environment was carried out by following the same procedure as Section 2.3, except that H_2O was replaced by D_2O.

2.5 Device applications

Toward future-oriented applied technology, two devices were assembled to assess practical potential of the catalysts. Flow cell reactor is equipped with gas diffusion electrode that enables direct contact between CO_2 and catalyst. Zn–CO_2 battery (ZCB) consists of Zn plate as anode, catalyst as cathode, and bipolar membrane

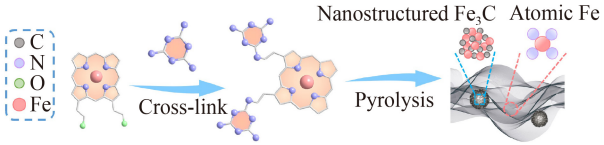

Fig. 1 Synthetic route of Fe_3C-X@Fe-NC.

separating anolyte and catholyte. Fabricating details and operating parameters are given in Texts S11 & S12 (cf. ESM).

3 Results and discussion

3.1 DFT calculation

DFT calculations for SA-Fe and A/N-Fe are performed to check the feasibility and disclose the structure-activity relationship (Fig. 2). Fe_3C, in view of its ferromagnetism able to impose exchange field and concomitantly long-range magnetic ordering on graphene via proximity effect [20,21], could endow Fe–N–C with some charming electronic properties desirable for proton utilization (Fig. 2(a)). Compared with SA-Fe, the local density of states (LDOS) projected on *d*-shell of the Fe center in A/N-Fe slightly extends and spreads toward low-energy side, with a tail emerging at the bottom edge (Fig. 2(b)). This phenomenon is derived from, in brief, proximity-induced spin polarization accompanying an exchange splitting that, to accommodate more polarized electronic states, compels *d*-levels to move below Fermi level (E_F) as possible (Fig. 2(c)) [22,23]. Full interpretation is dealt with in ESM (Scheme S1, Figs. S2–S4, cf. ESM). The *d*-band center is thus downshifted moderately, which, according to *d*-band theory (Fig. 2(d); the more the filled antibonding states, the weaker the adsorption) [24,25], brings two benefits to reliable proton constraint, direct or

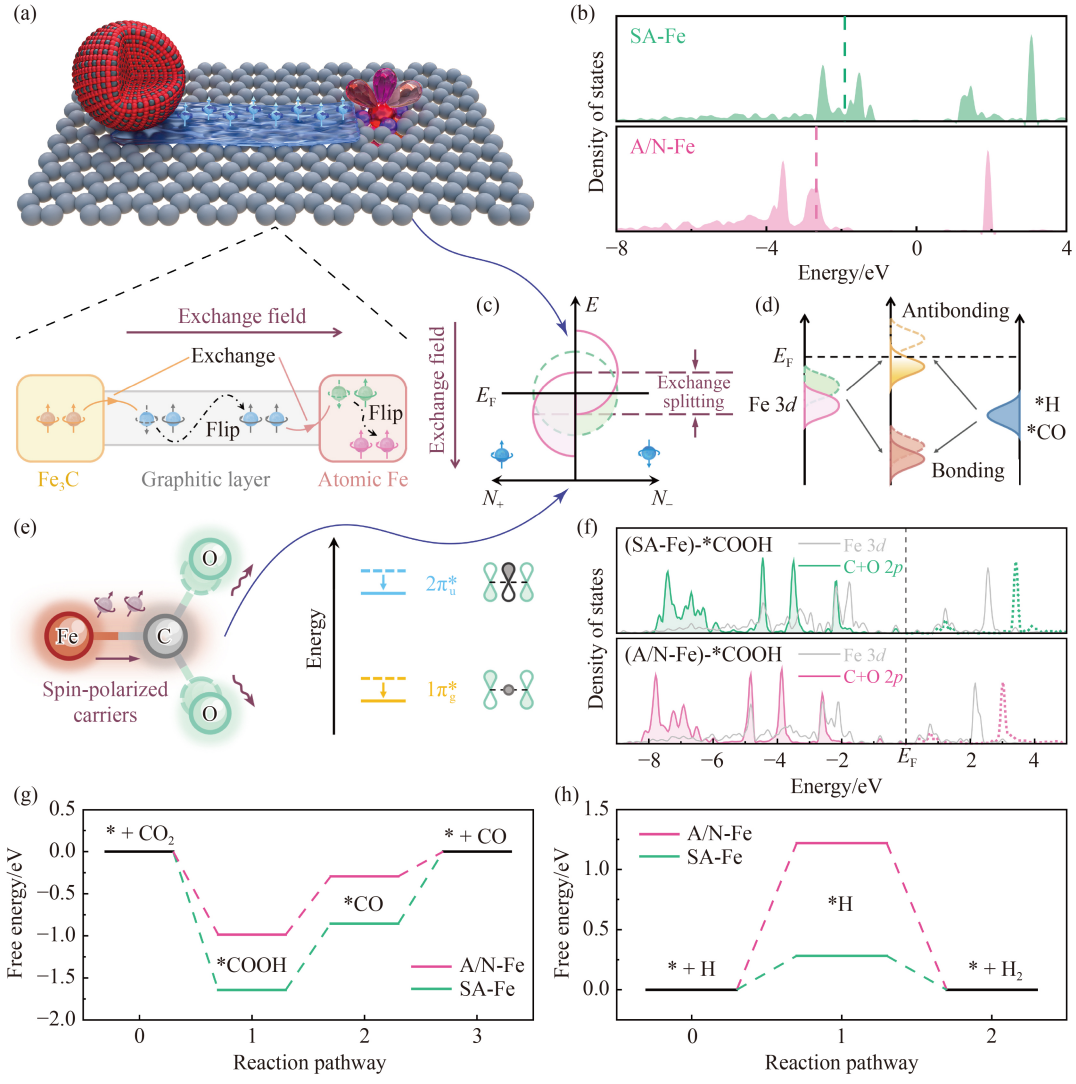

Fig. 2 Theoretical analysis of electronic structure and reaction path for SA-Fe and A/N-Fe. (a) Transport of the proximity-induced spin polarization by Fe_3C ferromagnet into anchored Fe site. (b) LDOS profiles projected on Fe 3d of the catalytic Fe sites; vertical dashed lines: *d*-band centers. (c) Exchange splitting that alters electron spins and energy levels of the entire system. (d) Metal-intermediate bond formation. (e) Changes in structural geometry and molecular orbital energies of a CO_2-relevant intermediate when accepting the spin-polarized carriers from the magnetic Fe site. (f) LDOS projected onto Fe 3d of the atomic Fe site and C & O 2p of the adsorbed COOH intermediate in (SA-Fe)–*COOH and (A/N-Fe)–*COOH. Free energy diagrams of (g) CO_2RR and (h) HER.

indirect. The direct one is to hinder the adsorption of proton on Fe center, also shown by the Fe 3d-H 1s states acquiring less bonding overlapping in (A/N-Fe)–*H LDOS (Fig. S5, cf. ESM). The highly-uplifted endergonic formation of Fe–*H helps cut off the Volmer step in HER course (Fig. 2(h)). The indirect one is to loosen the tight attachment of site-blocking *CO at Fe center, reducing the barrier for CO desorption (Fig. 2(g)). Active sites liable to be freed can trigger immediately a new round of CO_2 molecules stand-by for reduction, where protons are urgently needed, so that protons may be depleted with higher turnover rate down to a degree scarcely exploited for HER.

Deeper structure elucidation focused on *COOH, a key CO_2-relevant intermediate, identifies the π* antibonding population as a good descriptor to calibrate the difficulty of proton attack (see Scheme S2 (cf. ESM) for in-depth deduction). Spin-selected migration of the carriers between the magnetic A/N-Fe and the adsorbed *COOH will polarize the latter's *p*-levels (Fig. 2(e)) [26,27]. Its π* features, in response to the resultant exchange splitting induced inside its molecular orbitals, shift down and approach the E_F (Fig. 2(f)), gaining thereby more accessibility for external electrons to enter and occupy. The easier the filling of *COOH's π* antibonding orbitals, the more vulnerable the C–O bond [28,29], so the more its exposure to battering-breaking from protons (Scheme S2). Correspondingly, the energy ladder for *COOH → *CO descends by ~0.1 eV (Fig. 2(g)). Now, Fe_3C has proved theoretically successful in guiding protons to choose right path at the crossroads of this parallel reaction (CO_2RR vs. HER).

3.2 Physical characterization

The above A/N-Fe model is then constructed on a real Fe–N–C system, Fe_3C-X@Fe-NC. Micromorphology and composition of the Fe_3C-L@Fe-NC exemplar are presented in Fig. 3. Transmission electron microscopy (TEM) photographs the sample composed of thin, flocculent carbon nanosheets evenly decorated with dark nanoparticles (Fig. 3(a)). High-resolution TEM (HRTEM) image for a typical nanoparticle observes its decent crystallinity with lattice spacing of 0.24 and 0.16 nm in two directions at a characteristic angle of 70.7°, corresponding to Fe_3C (021) and (104), respectively (Fig. 3(b)). X-ray diffraction (XRD) spectrum further confirms the crystal phase (Fig. 3(c)). The diffraction peak at 26.4° corresponds to graphite (002), and the others from 37.7° to 78.8° are indexed to Fe_3C (JCPDS #76-1877). Raman spectrum shows clear D-band and G-band with I_D/I_G value of 0.72, indicating a good graphitization (Fig. S6, cf. ESM). N_2 adsorption/desorption isotherms show that the nanosheets are rich in mesopores (Fig. S7, cf. ESM), through which the transport of electrolyte and CO_2 can be facilitated. Energy dispersive X-ray spectroscopy (EDS) mapping images (Fig. 3(d)) display uniform N doping into the carbon matrix. Most of the Fe signals gather in nanoparticle region (white spot), and the rest are distributed discretely and overlap with N signals,

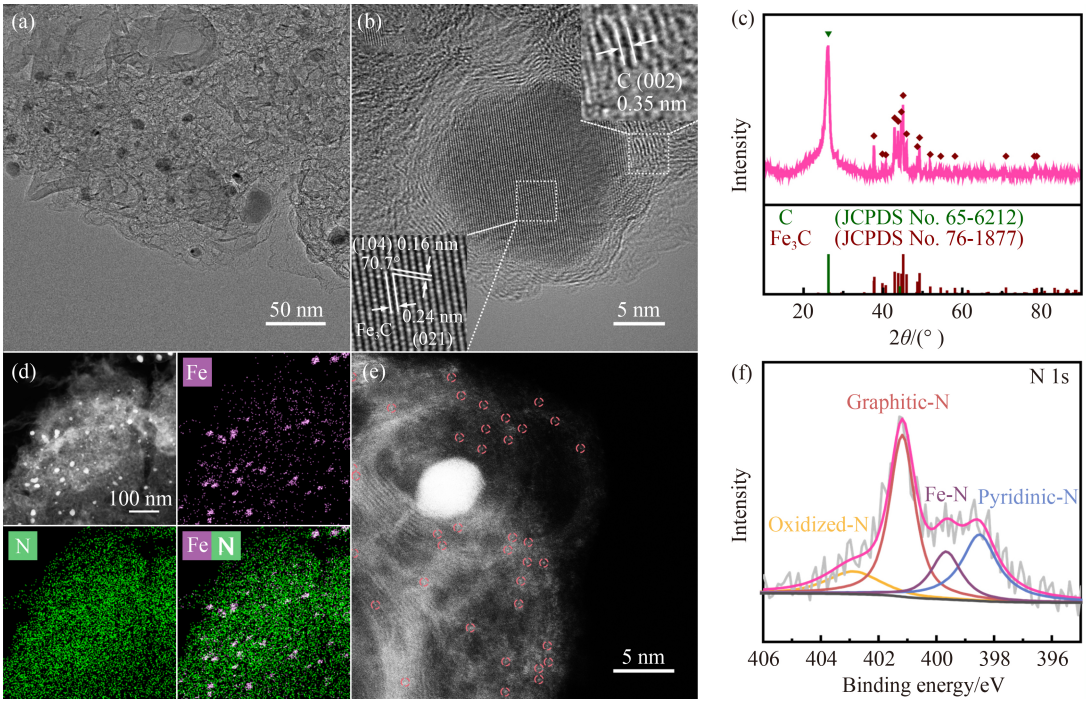

Fig. 3 Physical characterizations for Fe_3C-L@Fe-NC. (a) TEM image; (b) HRTEM image; insets: index crystal planes of graphite (top-right) and Fe_3C (bottom-left); (c) XRD spectrum; (d) EDS elemental mapping images; (e) AC-HAADF-STEM image; (f) XPS N 1s spectrum.

depicting the intimate intergrowth of Fe_3C nanoparticles and Fe-N_x sites [30,31]. Aberration-corrected high-angle annular dark-field scanning transmission electron microscopy (AC-HAADF-STEM) images further substantiate the existence of isolated Fe atoms (bright dots) closely adjacent to Fe_3C nanoparticles at nanoscale (Fig. 3(e); Fig. S8, cf. ESM). Such environment would favor the interaction between Fe-N_x and Fe_3C. Deconvoluted X-ray photoelectron spectroscopy (XPS) N 1s spectrum exhibits four types: pyridinic N (398.5 eV), Fe-N (399.7 eV), graphitic N (401.2 eV), and oxidized N (402.9 eV), verifying the N coordination in Fe-N_x moieties (Fig. 3(f)) [30–32].

To dig into the evolvement of A/N-Fe configuration, N_{Fe}/A_{Fe} is tuned by altering calcination parameters to obtain Fe_3C-M@Fe-NC, Fe_3C-S@Fe-NC, and Fe-NC (Figs. S9–S12, cf. ESM). XPS Fe 2p spectra suggest that the Fe peak of Fe-N_x moiety shifts to higher binding energy alongside Fe_3C generation (Fig. S13, cf. ESM), which might be a hint of interaction within the A/N-Fe pairs [30,31]. Quantitative analysis using XPS, inductively coupled plasma mass spectrometry and thermogravimetry gives the atomic Fe content decreasing down the series: Fe-NC > Fe_3C-S@Fe-NC > Fe_3C-M@Fe-NC > Fe_3C-L@Fe-NC, and this trend is reversed for nanostructured Fe_3C (Figs. S14–S16, cf. ESM; Tables S1 & S2, cf. ESM). Finally, FeC@C and NC are prepared as control samples (Figs. S17–S19, cf. ESM).

3.3 Electrochemical CO_2RR performance

Electrocatalytic performances of Fe_3C-X@Fe-NCs and Fe-NC are presented in Fig. 4. From on-line gas chromatography, gas product comprises only CO and H_2 (Fig. S20, cf. ESM), and no liquid product is detected by off-line ^1H nuclear magnetic resonance (Fig. S21, cf. ESM). Fe_3C-L@Fe-NC exhibits an impressively wide potential window for FE_{CO} > 90% from –0.34 to –0.64 V, spanning almost kinetics- and transfer-controlled region; the maximum reaches 98.1% at –0.4 V. By comparison, that of Fe_3C-M@Fe-NC, Fe_3C-S@Fe-NC and Fe-NC is 91.9%, 84.7% and 77.0%, respectively (Fig. 4(a)). Once the Fe-N_x sites are poisoned by SCN^-, Fe_3C-L@Fe-NC and Fe-NC suffer severe performance damage (Fig. S22, cf. ESM). Moreover, FeC@C has near-zero FE_{CO}; NC has a maximal FE_{CO} of only 58.1% with negligible current (Fig. S23, cf. ESM). These results confirm that Fe-N_x is the actual active center and Fe_3C itself is the spectator, and also that the co-existence of atomic Fe and nanostructured Fe_3C is essential for efficient CO_2 electrolysis. Fe_3C-X@Fe-NCs possess larger electrochemical active surface area (Fig. S24, cf. ESM) and smaller charge-transfer resistance (Fig. S25, cf. ESM) than Fe-NC. Among all the catalysts, Fe_3C-L@Fe-NC responds most sensitively to CO_2RR, as seen from the clearest cathodic peak and the lowest onset potential of –0.20 V for CO yielding (Fig. S26, cf. ESM). Tafel plots uncover the distinct kinetics (Fig. S27, cf. ESM): Fe_3C-L@Fe-NC experiences the fastest CO_2 activation step to generate $*CO_2^{\bullet-}$, explaining its lowest onset overpotential, followed by Fe_3C-M@Fe-NC and Fe_3C-S@Fe-NC, whereas Fe-NC suffers from the first PCET slow and rate-limiting [33]. For Fe_3C-L@Fe-NC, the CO partial current density (J_{CO}, Fig. 4(b)) and the turnover frequency (TOF, Fig. 4(c)) at –0.7 V are 3.5 mA·cm^{-2} and 193 h^{-1}, respectively, 3.5 and 16.1 times higher than Fe-NC—the optimal A/N-Fe

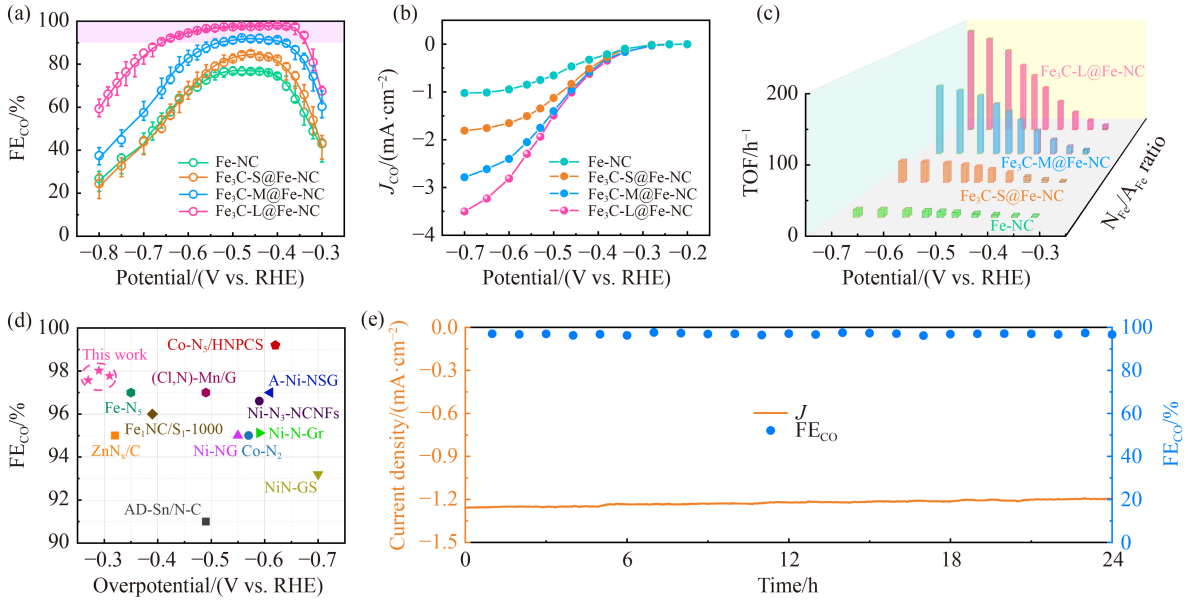

Fig. 4 Electrochemical CO_2RR performances of Fe_3C-X@Fe-NCs and Fe-NC. (a) FE_{CO}; (b) J_{CO}; (c) TOFs; (d) optimal FE_{CO} of Fe_3C-L@Fe-NC in comparison with other carbon-supported non-precious TM-N SACs; (e) long-term chronoamperometry curve and time-dependent FE_{CO} plot of Fe_3C-L@Fe-NC at –0.50 V.

configuration of Fe_3C-L@Fe-NC determines its order-of-magnitude enhancement in intrinsic activity. Marvelously, this hybrid catalyst with ultrahigh FE_{CO} at low overpotentials of 270–310 mV even surpasses manifold state-of-the-art M–N–C SACs (Fig. 4(d); Table S3, cf. ESM). Fe_3C-L@Fe-NC also keeps robust during 24 h continuous electrolysis, with steady current density (decay < 5%) and nearly constant FE_{CO} (~97%) (Fig. 4(e)), which is not shared by Fe-NC (Fig. S28, cf. ESM). After durability test, A/N-Fe pairs are still preserved intact (Fig. S29, cf. ESM).

To remove mass-transport limitation of the low-soluble CO_2 in H-cell [4,34], flow cell is then operated for scale-up electrolysis (Fig. S30, cf. ESM). Setting 90% FE_{CO} as dividing line, Fe_3C-L@Fe-NC bears an appreciable workload of 50 $mA \cdot cm^{-2}$ (Fig. S31, cf. ESM), equating to a CO production rate (r_{CO}) of 0.85 $mmol \cdot h^{-1} \cdot cm^{-2}$ (Fig. S32, cf. ESM).

3.4 *In situ* ATR-SEIRAS

To probe the microscopic origin behind A/N-Fe's impact on CO_2RR kinetics, *in situ* ATR-SEIRAS is employed to detect interfacial substances or functional groups and to monitor their evolutionary process and structural change. Peak positions and assignments are listed in Table S4 (cf. ESM). In the spectra collected along minus potentials, positive peaks signify a generation or increase of certain species and vice versa [35,36]. CO_2 and *COOH on the surface of either Fe-NC or Fe_3C-L@Fe-NC are being consumed and accumulated from –0.1 to –1.0 V, respectively (Fig. 5). The CO_2 consumption peaks in Fe_3C-L@Fe-NC are perceived to be bolder and appear ahead at lower potentials, indicating a much faster CO_2 activation consistent with Tafel plots. Noteworthily, the growth rate of the characteristic peaks associated with *COOH (O–H deformation, C–O and C=O stretching) is fairly accelerated in Fe_3C-L@Fe-NC (Fig. S33, cf. ESM), implying that A/N-Fe can better scavenge protons for rapid $*CO_2^{\bullet-} \rightarrow$ *COOH.

For a given unit in the species studied, its characteristic vibrational frequency reflects its geometric strength: long bond length adopts low frequency and vice versa [37,38]. The ν(C=O) and ν(C–O) over Fe_3C-L@Fe-NC slightly red-shifts relative to Fe-NC, in reasonable accord with the preceding theoretical section that invokes more π* electrons being injected into *COOH (owing to the π* orbitals pulled downward in energy) through A/N-Fe [39]. In this way, the rigid C–O bond is relaxed, and *COOH becomes thus prone to receive proton and lose oxygen. Notice that, as the reaction continues, the ν(C–O) over Fe-NC significantly blue-shifts, suggesting that SA-Fe may no longer afford the rising impetus (from the π* electrons) required to elongate C–O bond of the *COOH with rising coverage. Interestingly, A/N-Fe (only minor shift) hardly slackens off this weakening for the bond, which well preserves the exclusive access of protons to *COOH → *CO, and ensures they can still be utilized normally and progressively.

3.5 KIE study

To reveal the fine details of how A/N-Fe manipulates protons' behavior during CO_2RR, KIE evaluations are conducted in alternate protic (H_2O) and deuterated (D_2O) electrolytes (Fig. 6). Due to the lessened water dissociation by larger atomic mass of D than H, available concentration of D^+ in D_2O is relatively limited as against H^+ in H_2O [40]. In proton-poor D_2O, FE_{CO} is near-unity for both Fe-NC (96.6%–97.8%) and Fe_3C-L@Fe-NC (98.4%–99.2%) over a vast potential range (Fig. 6(a)), implying these finite D^+ ions inclined to preferentially supply to CO_2-relevant intermediates for the forthcoming transformation, whereby few remnants are ready for HER [13,41]. In proton-rich H_2O, however, maximal FE_{CO} of Fe-NC drastically drops to ~76%; HER intensifies,

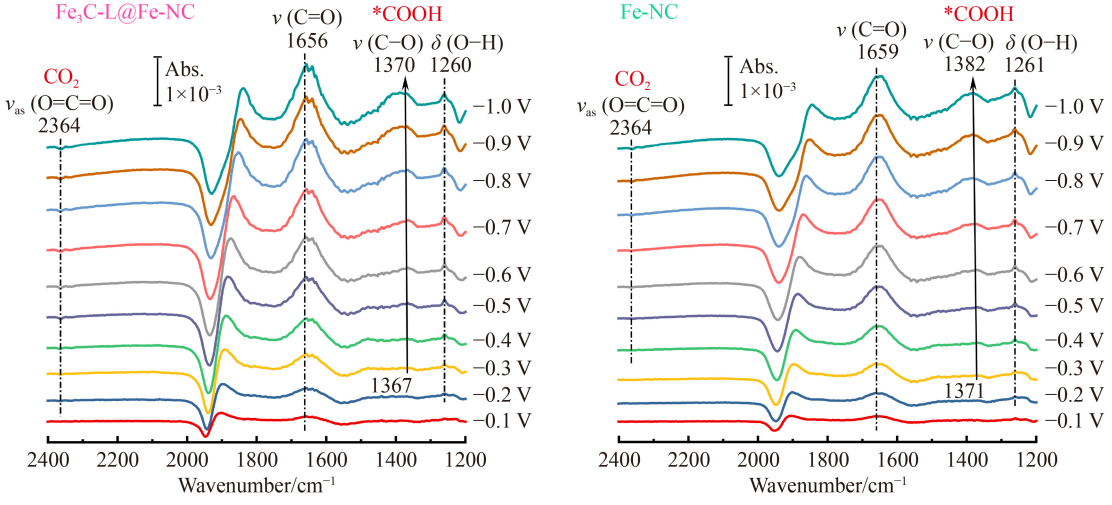

Fig. 5 Analysis of CO_2RR kinetics via *in situ* ATR-SEIRAS spectra.

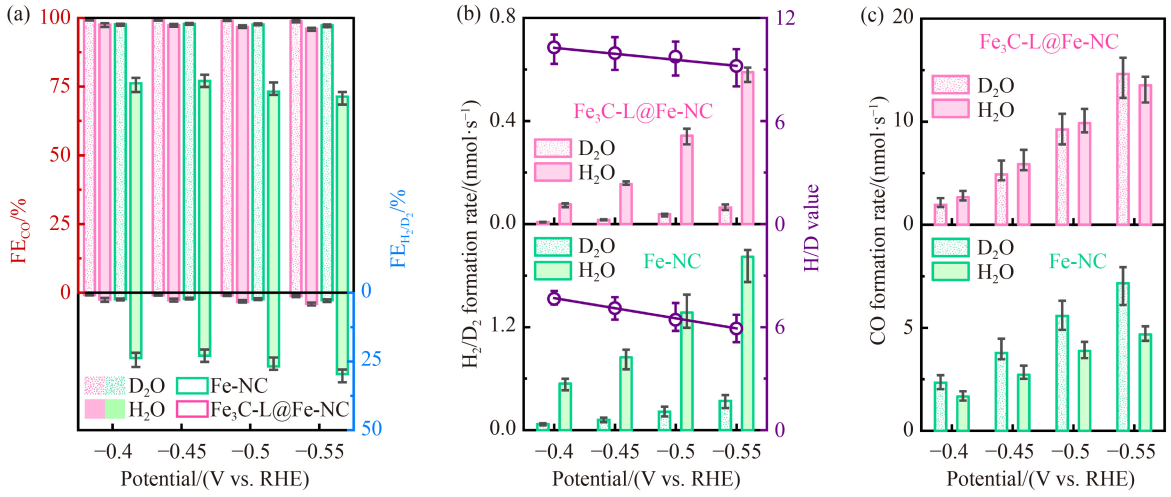

Fig. 6 KIE evaluations on CO_2RR and HER in protic and deuterated electrolytes. (a) FE of CO and H_2/D_2; (b) H_2/D_2 formation rates with the corresponding KIE values; (c) CO formation rates under different proton conditions.

violently. This phenomenon presumably arises from the substantial free H^+ ions not used up by CO_2RR going over to H_2 on Fe-NC, which lacks facility of proton regulation. In sharp contrast, Fe_3C-L@Fe-NC behave quite similarly to that in D_2O, maintaining adequately the high-level FE_{CO} with only ~2% reduction. Consequently, A/N-Fe is proposed capable of capturing or suppressing the excessive protons to avert their involvement in HER. Evidence is extracted from the KIE plots of hydrogen evolution during CO_2RR (Fig. 6(b)), in which all the H/D values of Fe_3C-L@Fe-NC are larger than Fe-NC, validating that the competing HER is kinetics-inhibited in the presence of A/N-Fe [42,43]. Notice that H/D value decreases with negative potential, since HER is severer under enhanced electrical driving force [44,45]. Interestingly, for Fe_3C-L@Fe-NC, HER-potential response diminishes, discerned from the gentler downward trend of H/D value vs. potential (see slopes of the fitted lines in Fig. 6(b)). It manifests that A/N-Fe can effectively alleviate HER's aggravation at larger overpotential, explaining the rather wider window for optimal FE_{CO} in Fe_3C-L@Fe-NC.

Once switched to proton-rich environment, CO production depends more deeply on whether or not "proton controller", A/N-Fe, is installed (Fig. 6(c)). When D_2O is replaced by H_2O, r_{CO} of Fe-NC abnormally declines, since plentiful unfettered protons escalate HER that then "seizes" the sites and electrons; the parallel CO_2RR is thus crowded out. On the contrary, r_{CO} of Fe_3C-L@Fe-NC rises over a certain range, driven by the well-controlled protons that correctly increase at the left side of CO_2 protonation steps (i.e., forward equilibrium obeying Le Chatelier's principle). Clearly, only if enough constraint on proton dynamics is attained, adding sufficient proton resource is conducive to higher yield of the expected product (CO_2RR); otherwise, just the opposite (HER).

3.6 Role of A/N-Fe in CO_2RR

The above analyses complete the picture of Fe_3C-L@Fe-NC's superiority attributable to the synergistic architecture of atomic-iron actors and nanostructured-iron assistors. There might be a combination of interactions between Fe_3C and, respectively, atomic Fe and graphitic layer [30,31,46,47], which establishes a favorable pattern of free energy on the catalytic system for electron transfer from Fe center to CO_2 (Scheme S3, cf. ESM), crucial for the smooth activation. The fact that the ensuing *COOH accepts more charge density donated by A/N-Fe provides a side argument (Fig. S2, cf. ESM). By magnetic-proximity spin polarization to modify some decisive factors—adsorption and bond reshaping toward the intermediates, A/N-Fe paves a streamlined, directional delivery of the required protons to, both the up- and down-river, PCETs, overcoming the sluggish ones stubborn of pristine SA-Fe (Scheme S4, cf. ESM). This is a seductive skill, the more so when A/N-Fe meanwhile restrains the superfluous part away from detrimental HER. No doubt, balance of protons will swing remarkably to CO_2RR, managing its quick start-up and efficient running (Fig. 7).

3.7 Rechargeable ZCB

For demonstration of practical application, Fe_3C-L@Fe-NC or Fe-NC is used to equip an aqueous rechargeable ZCB (Fig. 8), an appealing, multi-functional energy conversion device that integrates CO production with electricity output (Fig. 8(a)). At the cathode, CO_2RR or oxygen evolution reaction (OER) occurs during discharging or charging, respectively [48,49]. Fe_3C-L@Fe-NC boasts far more excellent battery performance than Fe-NC. Polarization curve gives a peak power density of 1.61 $mW \cdot cm^{-2}$ (Fig. 8(b)). Each applied

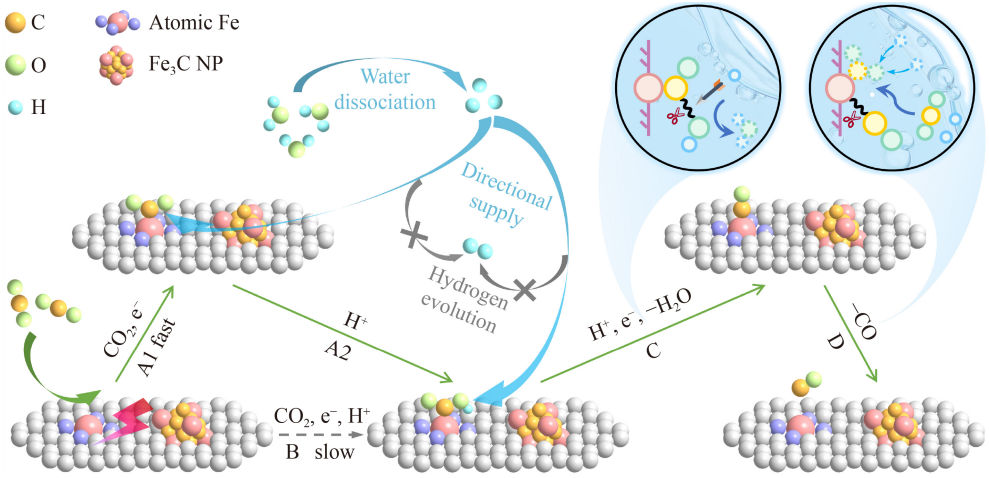

Fig. 7 Proposed mechanism of the proton dynamics optimized by A/N-Fe during CO_2 electrolysis.

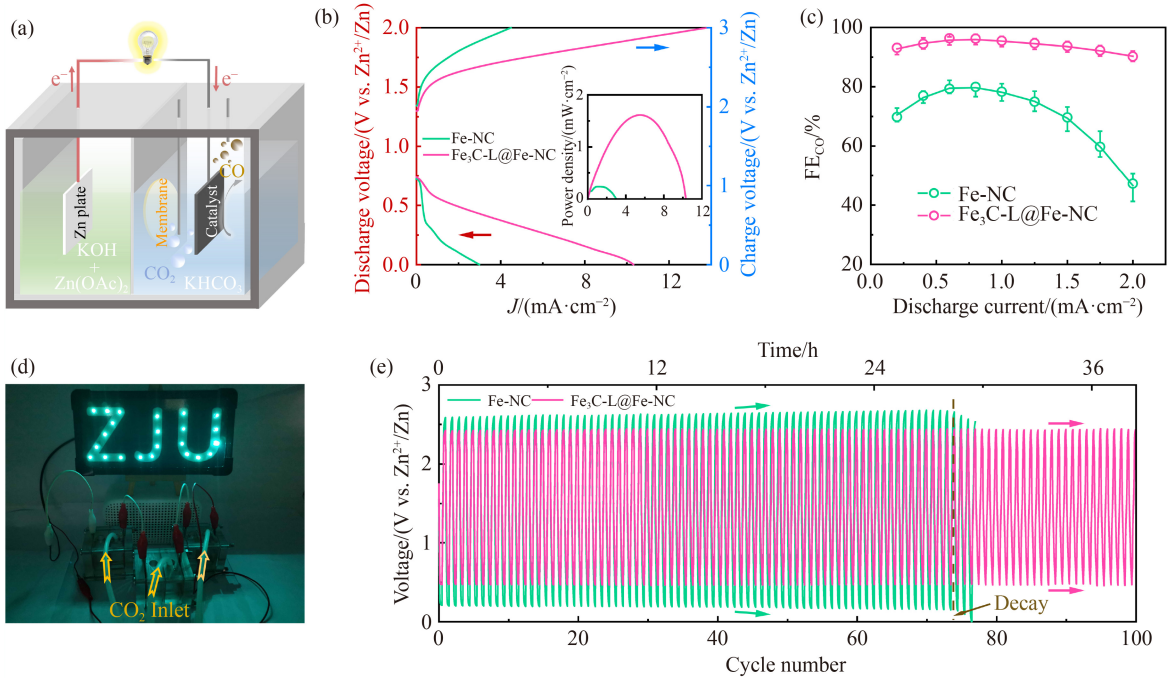

Fig. 8 Device performances of the assembled ZCBs. (a) Schematic of a ZCB. (b) Discharge and charge polarization curves; inset: power density profiles. (c) FE_{CO} upon ZCB discharging at varying constant-currents. (d) Digital photograph of an LED array lighted up by Fe_3C-L@Fe-NC–equipped ZCBs in serial connection. (e) Galvanostatic discharge/charge cycling curves at 1.0 mA·cm^{-2}.

constant-current point holds a higher discharge- and lower charge-voltage (Fig. S34, cf. ESM), meaning powerful output and convenient input. On primary cell mode, CO_2-to-CO dominates the cathodic compartment, with selectivity > 90% over a current range of 0.2–2.0 mA·cm^{-2} (Fig. 8(c)). Three series-connected ZCBs can illuminate a patterned array of light-emitting diodes (LEDs) brightly (Fig. 8(d)). The ZCB also possesses lengthy life spans, exhibiting a narrow, stable voltage gap (~1.96 V) during continuous galvanostatic discharge/charge cycling of up to 200 cycles (Fig. 8(e); Fig. S35, cf. ESM). Obviously, apart from CO_2RR, A/N-Fe with nanostructured Fe_3C boosts OER as well (Fig. S36, cf. ESM) [50], which qualifies Fe_3C-L@Fe-NC for a serviceable ZCB cathode that demands win−win situation of CO-electricity release (CO_2RR) and energy re-storage (OER) [48,49].

4 Conclusions

In summary, we have demonstrated a proton deployment strategy via A/N-Fe pairs constructed on N-doped carbon matrix, i.e., atomic Fe active centers with their inherent electronics tailored by nanostructured Fe_3C spin polarizer. Kinetic analyses clarify A/N-Fe's dual role in

the optimized CO_2 electrolysis: straight proton pathway to *COOH/*CO formation, and forceful proton constraint against H_2 evolution. CO_2 access and CO egress are also improved. All these merits, collectively, contribute to the overwhelming priority of CO_2RR over HER: a broad window (300 mV) for $FE_{CO} > 90\%$ (98% maximum). This well-planned "schedule" of proton dynamics offers a mechanistic guideline for SAC design, facilitating exploration of universal tools and methodologies regarding selective CO_2RR and even other electrocatalytic spheres (e.g., O_2/N_2 reduction), wherein protons, although tiny, profoundly affect the process and efficiency.

Acknowledgements We sincerely thank Dr. Guoqiang Shen (Tianjin University) for his multitude of instructive advice on theory, logic and particulars. This work was financially supported by National Natural Science Foundation of China (Grant Nos. 22075245, 21922811, 21878270, and 21961160742), Zhejiang Provincial Natural Science Foundation of China (Grant No. LR19B060002), Fundamental Research Funds for the Central Universities (Grant No. 2020XZZX002-09), Leading Innovative and Entrepreneur Team Introduction Program of Zhejiang (Grant No. 2019R01006), Startup Foundation for Hundred-Talent Program of Zhejiang University, Key Laboratory of Marine Materials and Related Technologies, Chinese Academy of Science, and Zhejiang Key Laboratory of Marine Materials and Protective Technologies (2020K10).

Electronic Supplementary Material Supplementary material is available in the online version of this article at https://dx.doi.org/10.1007/s11705-022-2197-4 and is accessible for authorized users.

References

1. Grim R G, Huang Z, Guarnieri M T, Ferrell J R, Tao L, Schaidle J A. Transforming the carbon economy: challenges and opportunities in the convergence of low-cost electricity and reductive CO_2 utilization. Energy & Environmental Science, 2020, 13(2): 472–494
2. Kortlever R, Shen J, Schouten K J P, Calle-Vallejo F, Koper M T M. Catalysts and reaction pathways for the electrochemical reduction of carbon dioxide. Journal of Physical Chemistry Letters, 2015, 6(20): 4073–4082
3. Birdja Y Y, Perez-Gallent E, Figueiredo M C, Gottle A J, Calle-Vallejo F, Koper M T M. Advances and challenges in understanding the electrocatalytic conversion of carbon dioxide to fuels. Nature Energy, 2019, 4(9): 732–745
4. Ross M B, De Luna P, Li Y, Dinh C T, Kim D, Yang P, Sargent E H. Designing materials for electrochemical carbon dioxide recycling. Nature Catalysis, 2019, 2(8): 648–658
5. Zhang Y J, Sethuraman V, Michalsky R, Peterson A A. Competition between CO_2 reduction and H_2 evolution on transition-metal electrocatalysts. ACS Catalysis, 2014, 4(10): 3742–3748
6. Cave E R, Shi C, Kuhl K P, Hatsukade T, Abram D N, Hahn C, Chan K, Jaramillo T F. Trends in the catalytic activity of hydrogen evolution during CO_2 electroreduction on transition metals. ACS Catalysis, 2018, 8(4): 3035–3040
7. Zheng T, Jiang K, Wang H. Recent advances in electrochemical CO_2-to-CO conversion on heterogeneous catalysts. Advanced Materials, 2018, 30(48): 1802066
8. Wang Y, Liu Y, Liu W, Wu J, Li Q, Feng Q, Chen Z, Xiong X, Wang D, Lei Y. Regulating the coordination structure of metal single atoms for efficient electrocatalytic CO_2 reduction. Energy & Environmental Science, 2020, 13(12): 4609–4624
9. Pan Y, Zhang C, Liu Z, Chen C, Li Y D. Structural regulation with atomic-level precision: from single-atomic site to diatomic and atomic interface catalysis. Matter, 2020, 2(1): 78–110
10. Zang W, Kou Z, Pennycook S J, Wang J. Heterogeneous single atom electrocatalysis, where "singles" are "married". Advanced Energy Materials, 2020, 10(9): 1903181
11. Jiao J, Lin R, Liu S, Cheong W C, Zhang C, Chen Z, Pan Y, Tang J, Wu K, Hung S F, Chen H M, Zheng L, Lu Q, Yang X, Xu B, Xiao H, Li J, Wang D, Peng Q, Chen C, Li Y. Copper atom-pair catalyst anchored on alloy nanowires for selective and efficient electrochemical reduction of CO_2. Nature Chemistry, 2019, 11(3): 222–228
12. Liu C, Wu Y, Sun K, Fang J, Huang A, Pan Y, Cheong W C, Zhuang Z, Zhuang Z, Yuan Q, Xin H L, Zhang C, Zhang J, Xiao H, Chen C, Li Y. Constructing FeN_4/graphitic nitrogen atomic interface for high-efficiency electrochemical CO_2 reduction over a broad potential window. Chem, 2021, 7(5): 1297–1307
13. Bondue C J, Graf M, Goyal A, Koper M T M. Suppression of hydrogen evolution in acidic electrolytes by electrochemical CO_2 reduction. Journal of the American Chemical Society, 2021, 143(1): 279–285
14. Ma W, Xie S, Zhang X G, Sun F, Kang J, Jiang Z, Zhang Q, Wu D Y, Wang Y. Promoting electrocatalytic CO_2 reduction to formate via sulfur-boosting water activation on indium surfaces. Nature Communications, 2019, 10(1): 892
15. Wang X, Sang X, Dong C L, Yao S, Shuai L, Lu J, Yang B, Li Z, Lei L, Qiu M, Dai L, Hou Y. Proton capture strategy for enhancing electrochemical CO_2 reduction on atomically dispersed metal-nitrogen active sites. Angewandte Chemie International Edition, 2021, 60(21): 11959–11965
16. Ju W, Bagger A, Hao G P, Sofia Varela A, Sinev I, Bon V, Roldan Cuenya B, Kaskel S, Rossmeisl J, Strasser P. Understanding activity and selectivity of metal−nitrogen-doped carbon catalysts for electrochemical reduction of CO_2. Nature Communications, 2017, 8(1): 944
17. Zhang H, Li J, Xi S, Du Y, Hai X, Wang J, Xu H, Wu G, Zhang J, Lu J, Wang J. A graphene-supported single-atom FeN_5 catalytic site for efficient electrochemical CO_2 reduction. Angewandte Chemie International Edition, 2019, 58(42): 14871–14876
18. Li J, Mao S, Hou Y, Lei L, Yuan C. 3D edge-enriched Fe_3C@C nanocrystals with a core-shell structure grown on reduced graphene oxide networks for efficient oxygen reduction reaction. ChemSusChem, 2018, 11(18): 3292–3298
19. Zhang W, Yin J, Sun M, Wang W, Chen C, Altunkaya M, Emwas A H, Han Y, Schwingenschlogl U, Alshareef H N. Direct pyrolysis of supermolecules: an ultrahigh edge-nitrogen doping strategy of carbon anodes for potassium-ion batteries. Advanced Materials, 2020, 32(25): 2000732
20. Shao Y, Pang R, Shi X. Stability of two-dimensional iron

carbides suspended across graphene pores: first-principles particle swarm optimization. Journal of Physical Chemistry C, 2015, 119(40): 22954–22960
21. Zutic I, Matos-Abiague A, Scharf B, Dery H, Belashchenko K. Proximitized materials. Materials Today, 2019, 22: 85–107
22. Stöhr J, Siegmann H C. Magnetism: From Fundamentals to Nanoscale Dynamics. Berlin: Springer, 2006: 235–240
23. Marder M P. Condensed Matter Physics. Hoboken: Wiley, 2010: 811–813
24. Norskov J K, Bligaard T, Rossmeisl J, Christensen C H. Towards the computational design of solid catalysts. Nature Chemistry, 2009, 1(1): 37–46
25. Zhao Z J, Liu S, Zha S, Cheng D, Studt F, Henkelman G, Gong J. Theory-guided design of catalytic materials using scaling relationships and reactivity descriptors. Nature Reviews Materials, 2019, 4(12): 792–804
26. Ren X, Wu T Z, Sun Y M, Li Y, Xian G Y, Liu X H, Shen C M, Gracia J, Gao H J, Yang H T, Xu Z J. Spin-polarized oxygen evolution reaction under magnetic field. Nature Communications, 2021, 12(1): 2608
27. Wu T Z, Ren X, Sun Y M, Sun S N, Xian G Y, Scherer G G, Fisher A C, Mandler D, Ager J W, Grimaud A, Wang J, Shen C, Yang H, Gracia J, Gao H J, Xu Z J. Spin pinning effect to reconstructed oxyhydroxide layer on ferromagnetic oxides for enhanced water oxidation. Nature Communications, 2021, 12(1): 3634
28. Demtröder W. Atoms, Molecules and Photons: An Introduction to Atomic-, Molecular- and Quantum Physics. Berlin: Springer, 2018: 320–322
29. Zhang X, Li X Q, Zhang D, Su N Q, Yang W T, Everitt H O, Liu J. Product selectivity in plasmonic photocatalysis for carbon dioxide hydrogenation. Nature Communications, 2017, 8(1): 14542
30. Jiang W J, Gu L, Li L, Zhang Y, Zhang X, Zhang L J, Wang J Q, Hu J S, Wei Z, Wan L J. Understanding the high activity of Fe-N-C electrocatalysts in oxygen reduction: Fe/Fe_3C nanoparticles boost the activity of $Fe\text{-}N_x$. Journal of the American Chemical Society, 2016, 138(10): 3570–3578
31. Hu J, Wang S, Yu J, Nie W, Sun J, Wang S. Duet Fe_3C and FeN_x sites for H_2O_2 generation and activation toward enhanced electro-Fenton performance in wastewater treatment. Environmental Science & Technology, 2021, 55(2): 1260–1269
32. Li J, Ghoshal S, Liang W, Sougrati M T, Jaouen F, Halevi B, McKinney S, McCool G, Ma C, Yuan X, Ma Z F, Mukerjee S, Jia Q. Structural and mechanistic basis for the high activity of Fe–N–C catalysts toward oxygen reduction. Energy & Environmental Science, 2016, 9(7): 2418–2432
33. Gu J, Hsu C S, Bai L, Chen H M, Hu X. Atomically dispersed Fe^{3+} sites catalyze efficient CO_2 electroreduction to CO. Science, 2019, 364(6445): 1091–1094
34. Burdyny T, Smith W A. CO_2 reduction on gas-diffusion electrodes and why catalytic performance must be assessed at commercially-relevant conditions. Energy & Environmental Science, 2019, 12(5): 1442–1453
35. Firet N J, Smith W A. Probing the reaction mechanism of CO_2 electroreduction over Ag films via operando infrared spectroscopy. ACS Catalysis, 2017, 7(1): 606–612
36. Zhu S, Jiang B, Cai W B, Shao M. Direct observation on reaction intermediates and the role of bicarbonate anions in CO_2 electrochemical reduction reaction on Cu surfaces. Journal of the American Chemical Society, 2017, 139(44): 15664–15667
37. Günzler H, Gremlich H U I R. Spectroscopy: an Introduction. Weinheim: Wiley, 2002: 14–16
38. Rankin D W H, Mitzel N W, Morrison C A. Structural Methods in Molecular Inorganic Chemistry. Chichester: Wiley, 2013: 237–238
39. Kettle S F A. Physical Inorganic Chemistry: A Coordination Chemistry Approach. Berlin: Springer, 1996: 229–230
40. Bell R P. The Proton in Chemistry. London: Chapman & Hall, 1973: 232–235
41. Goyal A, Marcandalli G, Mints V A, Koper M T M. Competition between CO_2 reduction and hydrogen evolution on a gold electrode under well-defined mass transport conditions. Journal of the American Chemical Society, 2020, 142(9): 4154–4161
42. Hammes-Schiffer S. Theory of proton-coupled electron transfer in energy conversion processes. Accounts of Chemical Research, 2009, 42(12): 1881–1889
43. Liu E, Jiao L, Li J, Stracensky T, Sun Q, Mukerjee S, Jia Q. Interfacial water shuffling the intermediates of hydrogen oxidation and evolution reactions in aqueous media. Energy & Environmental Science, 2020, 13(9): 3064–3074
44. Goldsmith Z K, Lam Y C, Soudackov A V, Hammes-Schiffer S. Proton discharge on a gold electrode from triethylammonium in acetonitrile: theoretical modeling of potential-dependent kinetic isotope effects. Journal of the American Chemical Society, 2019, 141(2): 1084–1090
45. Lam Y C, Soudackov A V, Hammes-Schiffer S. Theory of electrochemical proton-coupled electron transfer in diabatic vibronic representation: application to proton discharge on metal electrodes in alkaline solution. Journal of Physical Chemistry C, 2020, 124(50): 27309–27322
46. Deng D H, Yu L, Chen X Q, Wang G X, Jin L, Pan X L, Deng J, Sun G Q, Bao X H. Iron encapsulated within pod-like carbon nanotubes for oxygen reduction reaction. Angewandte Chemie International Edition, 2013, 52(1): 371–375
47. Hu Y, Jensen J O, Zhang W, Cleemann L N, Xing W, Bjerrum N J, Li Q. Hollow spheres of iron carbide nanoparticles encased in graphitic layers as oxygen reduction catalysts. Angewandte Chemie International Edition, 2014, 53(14): 3675–3679
48. Xie J, Wang Y. Recent development of CO_2 electrochemistry from $Li–CO_2$ batteries to $Zn–CO_2$ batteries. Accounts of Chemical Research, 2019, 52(6): 1721–1729
49. Wang X, Xie J, Ghausi M A, Lv J, Huang Y, Wu M, Wang Y, Yao J. Rechargeable $Zn–CO_2$ electrochemical cells mimicking two-step photosynthesis. Advanced Materials, 2019, 31(17): 1807807
50. Liang X, Xiao J, Weng W, Xiao W. Electrochemical reduction of carbon dioxide and iron oxide in molten salts to Fe/Fe_3C modified carbon for electrocatalytic oxygen evolution. Angewandte Chemie International Edition, 2021, 60(4): 2120–2124